RESEARCH ARTICLE

National Science Review
11: nwae252, 2024
https://doi.org/10.1093/nsr/nwae252
Advance access publication 23 July 2024

CHEMISTRY

Regulating interaction with surface ligands on Au_{25} nanoclusters by multivariate metal–organic framework hosts for boosting catalysis

He Wang[1,2,†], Xiaokang Liu[3,†], Yulong Zhao[1,2], Zhihu Sun[3], Yue Lin[1], Tao Yao[3,*] and Hai-Long Jiang[1,2,*]

ABSTRACT

While atomically precise metal nanoclusters (NCs) with unique structures and reactivity are very promising in catalysis, the spatial resistance caused by the surface ligands and structural instability poses significant challenges. In this work, $Au_{25}(Cys)_{18}$ NCs are encapsulated in multivariate metal–organic frameworks (MOFs) to afford Au_{25}@M-MOF-74 (M = Zn, Ni, Co, Mg). By the MOF confinement, the Au_{25} NCs showcase highly enhanced activity and stability in the intramolecular cascade reaction of 2-nitrobenzonitrile. Notably, the interaction between the metal nodes in M-MOF-74 and $Au_{25}(Cys)_{18}$ is able to suppress the free vibration of the surface ligands on the Au_{25} NCs and thereby improve the accessibility of Au sites; meanwhile, the stronger interactions lead to higher electron density and core expansion within $Au_{25}(Cys)_{18}$. As a result, the activity exhibits the trend of Au_{25}@Ni-MOF-74 > Au_{25}@Co-MOF-74 > Au_{25}@Zn-MOF-74 > Au_{25}@Mg-MOF-74, highlighting the crucial roles of microenvironment modulation around the Au_{25} NCs by interaction between the surface ligands and MOF hosts.

Keywords: metal nanoclusters, metal–organic frameworks, heterogeneous catalysis, microenvironment modulation

[1]Hefei National Research Center for Physical Sciences at the Microscale, University of Science and Technology of China, Hefei 230026, China; [2]Department of Chemistry, University of Science and Technology of China, Hefei 230026, China and [3]National Synchrotron Radiation Laboratory, University of Science and Technology of China, Hefei 230029, China

***Corresponding authors.** E-mails: yaot@ustc.edu.cn; jianglab@ustc.edu.cn

[†]Equally contributed to this work.

Received 25 May 2024; **Revised** 26 June 2024; **Accepted** 7 July 2024

INTRODUCTION

The design and fabrication of structurally precise metal sites are crucial for the development of high-performance heterogeneous catalysts [1–3]. Metal nanoclusters (NCs) with atomic-level structural precision have attracted intense attention due to their small size, uniform active sites and unique electronic structures, giving rise to outstanding activity and selectivity in various catalytic reactions [4–7]. Unfortunately, the surface of metal NCs is always covered with numerous organic ligands that substantially influence catalysis. On the one hand, these surface ligands are detrimental to the accessibility of metal sites [8,9]; on the other, they optimize the electronic structure of metal NCs and improve the activity and selectivity of specific reactions [10–12]. Therefore, the role of surface ligands is akin to a double-edged sword affecting the catalytic properties [13]. In this context, it would be of great importance to preserve the strength yet suppress the drawback of surface ligands on metal NCs, so as to promote the catalysis of metal NCs. Inspired by the crucial roles of the surrounding microenvironment around catalytic centers in bio-enzyme catalysis [14], through the manipulation of the organic surface ligands on metal NCs, it might be possible to improve the substrate accessibility to and electronic structure of catalytic metal sites. To this end, it would be highly desired to develop porous hosts featuring well-defined structures and tunable interaction with the surface ligands. This would allow the regulation of their configuration and movement, thereby influencing the accessibility and activity of central metal sites.

To achieve the aforementioned goal, metal–organic frameworks (MOFs)—a class of crystalline porous materials with coordinatively unsaturated metal sites (for interacting with surface ligands) and tunable pore sizes (for hosting metal NCs)—

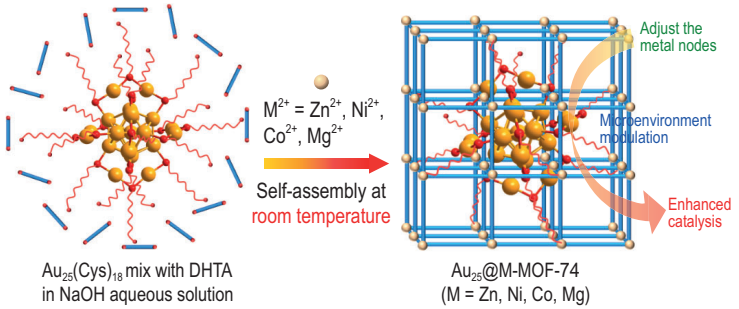

Figure 1. Illustration showing the synthetic route to Au_{25}@M-MOF-74 (M = Zn, Ni, Co, Mg) for enhanced catalysis through microenvironment modulation around $Au_{25}(Cys)_{18}$ by adjusting the metal nodes on MOF pore walls.

would be promising candidates [15–18]. MOFs have been demonstrated to be very suitable for incorporating diverse catalytically active species, including single-atom metal sites [19,20], metal nanoparticles [21,22], organic molecules [23], enzymes [24,25], etc., into pore spaces for enhanced catalysis. There have been also a couple of reports on the integration of metal NCs with MOFs in catalysis [26–31], where the regulation of surface ligands on metal NCs has not yet been investigated, except for ligand removal in the only study [32]. Given that the structure and properties of metal NCs are particularly sensitive to the surrounding microenvironment [33], it would be reasonable to adopt MOFs to modulate the microenvironment around metal NCs by regulating their surface ligands based on their interaction with MOFs for enhanced catalytic performance [34]. It is expected that the interactions between surface ligands of metal NCs and MOFs would effectively suppress the free vibration of surface ligands in solution and reduce their hindrance of substrate access to the metal sites [26]. Moreover, the spatial confinement effect of MOFs would significantly improve the catalytic stability of metal NCs [27–29]. However, to our knowledge, it remains unknown how the interaction with porous hosts (e.g. MOFs) regulates the surface ligands on metal NCs for improved catalysis.

In this work, $Au_{25}(Cys)_{18}$ NCs are encapsulated into representative multivariate MOFs, M-MOF-74 (M = Zn, Ni, Co, Mg), based on coordinated self-assembly and electrostatic interactions to afford Au_{25}@M-MOF-74 (Fig. 1). Significant differences in the fluorescence properties of $Au_{25}(Cys)_{18}$ are observed among these materials, which can be attributed to the restricted influence of M-MOF-74 encapsulation on the surface-ligand vibration behavior of $Au_{25}(Cys)_{18}$. Accordingly, the encapsulation of Au_{25} NCs in M-MOF-74 significantly improves its catalytic efficiency in the intramolecular cascade reaction of 2-nitrophenyl cyanide. Furthermore, X-ray absorption spectroscopy (XAS) results indicate that the electron density of $Au_{25}(Cys)_{18}$ and the length of the Au–Au bonds within the core of $Au_{25}(Cys)_{18}$ can be systematically regulated in addition to the interaction strengths between M-MOF-74 and $Au_{25}(Cys)_{18}$ NCs. Such interaction modulates the microenvironment of $Au_{25}(Cys)_{18}$, which improves the Au_{25} accessibility and facilitates the electron transfer from the Au_{25} NCs to substrates responsible for promoting the catalysis. As a result, the catalytic activity can be further regulated by doping the metal nodes of MOF-74 in the following sequence: Ni > Co > Zn > Mg. Moreover, Au_{25}@Ni-MOF-74 exhibits far superior catalytic activity and stability to the control of Au_{25}/Ni-MOF-74 that is made by supporting the Au_{25} NCs on the outer surface of Ni-MOF-74. As far as we know, this is the first report on regulating interaction by MOFs with surface ligands of metal clusters, resulting in enhanced catalysis.

RESULTS AND DISCUSSION

Synthesis and characterization of the Au_{25}@Ni-MOF-74 catalyst

The $Au_{25}(Cys)_{18}$ NCs were selected due to their relatively stable structure and abundance of carbonyl groups on the surface (Fig. S1a) [35]. It was synthesized by the NaOH-mediated $NaBH_4$ reduction method and the high purity of the synthesized $Au_{25}(Cys)_{18}$ was confirmed by using UV–vis spectroscopy and high-angle annular dark-field scanning transmission electron microscopy (HAADF-STEM) (Fig. S2) [35]. To prevent structural damage to $Au_{25}(Cys)_{18}$ under high-temperature solution conditions, *in situ* growth of the MOF-74 outer-shell was developed. The MOF linker, 2,5-dihydroxyterephthalic acid (DHTP) and $Au_{25}(Cys)_{18}$ were pretreated in aqueous NaOH solution, inducing the deprotonation and subsequently promoting the dissolution of DHTP in water. This facilitates the reaction with metal ions, leading to the growth of MOF at room temperature, and promotes the dispersion and encapsulation of $Au_{25}(Cys)_{18}$ in MOF-74. Subsequently, the metal ions underwent coordination self-assembly with $Au_{25}(Cys)_{18}$ and DHTP at room temperature, resulting in the formation of Au_{25}@MOF-74 [36]. Taking advantage of the multivariate feature of MOFs, M-MOF-74 (M = Ni, Co, Mg) with Ni^{2+}, Co^{2+} or Mg^{2+} in the Zn-oxo chains was obtained (Fig. S1b), ensuring their similar crystallinity and sizes, by mixing these metal acetates together with zinc acetate in the synthesis of Zn-MOF-74. Accordingly, Au_{25}@M-MOF-74 (M = Zn, Ni, Co, Mg) were fabricated following a similar synthetic route to Au_{25}@MOF-74, which

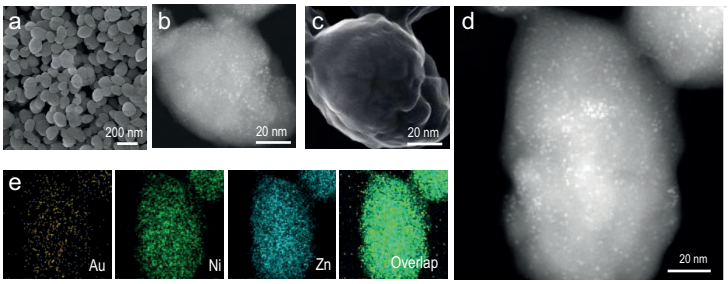

Figure 2. (a) SEM image, (b) HAADF-STEM and (c) the corresponding SE-STEM image of Au_{25}@Ni-MOF-74. (d) HAADF-STEM image and (e) corresponding EDS elemental mapping of Au, Ni and Zn, and their overlap for Au_{25}@Ni-MOF-74.

would serve as an ideal platform for regulating the interaction with the surface ligands of $Au_{25}(Cys)_{18}$. In addition, due to the presence of a large number of negatively charged carboxyl groups on the surface, $Au_{25}(Cys)_{18}$ can be attached to the outer surface of Ni-MOF-74 by electrostatic interaction to yield $Au_{25}(Cys)_{18}$/Ni-MOF-74 [30,31].

Powder X-ray diffraction (XRD) patterns indicate that the M-MOF-74 has similar crystallinity and $Au_{25}(Cys)_{18}$ encapsulation or support has no influence on the structural integrity and crystallinity of the MOFs (Fig. S3). Nitrogen sorption results demonstrate that Au_{25}@M-MOF-74 and Au_{25}/Ni-MOF-74 maintain the high porosity and very similar pore size distribution, indicating that the introduction of $Au_{25}(Cys)_{18}$ does not affect the MOF microporous structure (Fig. S4). The Brunauer-Emmett-Teller surface area of Au_{25}@Ni-MOF-74 is 639 m^2/g, similar to that of Au_{25}@Zn-MOF-74 (604 m^2/g), Au_{25}@Co-MOF-74 (609 m^2/g) and Au_{25}@Mg-MOF-74 (610 m^2/g), reflecting that different metal nodes have little influence on the surface area. Due to the pore space occupation of MOF-74 by the Au_{25} NCs, their surface areas are reasonably lower than Au_{25}/MOF-74 (667 m^2/g). For Au_{25}@M-MOF-74, $Au_{25}(Cys)_{18}$ can be isolated by the removal of MOF-74 using dilute hydrochloric acid. UV–vis spectra for the isolated $Au_{25}(Cys)_{18}$ NCs, upon removing the MOF, showcase the characteristic bands (Fig. S5), demonstrating that MOF-74 encapsulation does not influence the integrity of the $Au_{25}(Cys)_{18}$ structure.

Scanning electron microscopy (SEM) images show that Au_{25}@M-MOF-74 and Au_{25}/Ni-MOF-74 have similar particle sizes and morphology (Fig. 2a and Fig. S6). From the high-angle annular dark-field-scanning transmission electron microscopy (HAADF-STEM) images, it can be observed that $Au_{25}(Cys)_{18}$ NCs are uniformly dispersed throughout the Ni-MOF-74 support (Fig. 2b and Fig. S7a). Direct comparison of the HAADF-STEM and secondary electron STEM (SE-STEM) images acquired at the same location provides direct evidence that $Au_{25}(Cys)_{18}$ NCs are encapsulated inside Ni-MOF-74 in Au_{25}@Ni-MOF-74, as indicated by unobservable Au_{25} NCs in the SE-STEM image (Fig. 2b and c). By comparison, the Au_{25} NCs can be clearly observed in both images, showing that the Au_{25} NCs are supported on the surface of Ni-MOF-74 in Au_{25}/Ni-MOF-74 (Fig. S8). HAADF-STEM images of Au_{25}@Ni-MOF-74 projected at different tilt angles (from +30° to −30°) show that the Au_{25} NCs remain monodispersed in the Ni-MOF-74 (Fig. S9). The HAADF-STEM images and corresponding energy dispersive X-ray spectroscopy (EDS) mapping analyses reveal that both metals in M-MOF-74 and $Au_{25}(Cys)_{18}$ are uniformly distributed throughout the MOF particle (Fig. 2d and e, and Figs S9–S12). The Au loading amount in Au_{25}@M-MOF-74 is controlled to be ∼2 wt% and the mixed metal molar ratio in M-MOF-74 is also maintained at ∼1 according to inductively coupled plasma atomic emission spectroscopy (ICP-AES) results (Table S1).

Performance of catalytic reduction of 2-nitrobenzonitrile

Given the unique surface and electronic structure of $Au_{25}(Cys)_{18}$ NCs, they can serve as electron mediators to initiate catalysis via single electron transfer [37,38]. Therefore, the reduction reaction of 2-nitrobenzonitrile containing electron-transfer processes is adopted, which is an important route for the production of significant pharmaceuticals precursor 2-amniobenzamide [37]. Control experiments indicate that no product is detected in the absence of catalysts or with the use of the four M-MOF-74 catalysts (Table S2). When adopting $Au_{25}(Cys)_{18}$ NCs, the activity and selectivity are 20.6% and 91.0%, respectively, indicating that the Au_{25} NCs are able to behave as active species. Unfortunately, they are prone to aggregation, as supported by the UV–vis spectrum and HAADF-STEM observation (Fig. S13). Moreover, no obvious difference in catalytic activity is observed when the same amount of Au_{25} NCs is physically mixed with the four M-MOF-74, respectively, indicating that M-MOF-74 does not affect the catalytic reaction process (Table S2).

Strikingly, the encapsulation of $Au_{25}(Cys)_{18}$ NCs in M-MOF-74 significantly improves the activity, in which the conversion and selectivity reach 99.8% and 99.2%, respectively, for Au_{25}@Ni-MOF-74 (Fig. 3a). In comparison, the conversion and selectivity of Au_{25}@Co-MOF-74, Au_{25}@Zn-MOF-74 and Au_{25}@Mg-MOF-74 are decreased, with conversion of 72.7%, 46.2% and 32.1%, and selectivity of 97.1%, 94.3% and 93.5%, respectively (Fig. 3a).

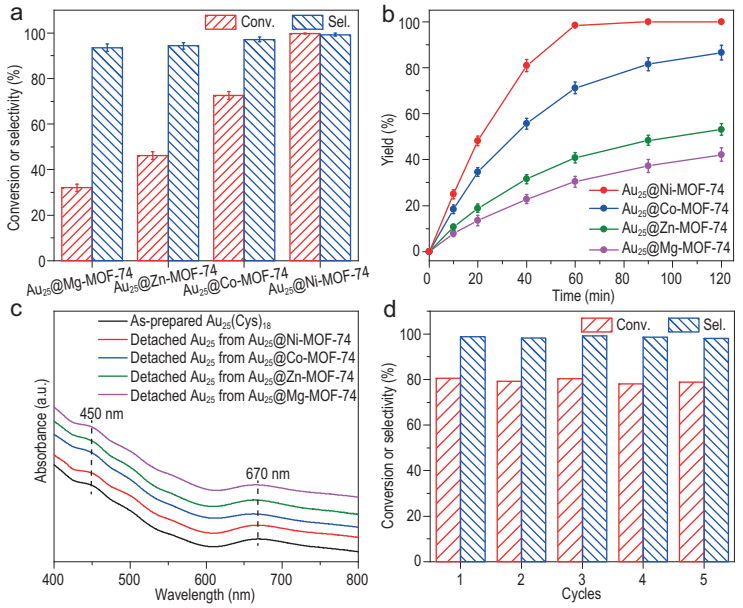

Figure 3. (a) The conversion and selectivity of Au_{25}@M-MOF-74 (~2 wt% Au loading) in the intramolecular cascade reaction of 2-nitrobenzonitrile at 25°C for 1 h. (b) Time-dependent yield of 2-aminobenzamide with Au_{25}@M-MOF-74. (c) UV–vis spectra of as-prepared $Au_{25}(Cys)_{18}$ and the $Au_{25}(Cys)_{18}$ NCs detached from Au_{25}@M-MOF-74 after the catalytic reaction. (d) The recyclability tests of Au_{25}@Ni-MOF-74.

The reaction yield gradually increases along with reaction time, showcasing activity in the order of Au_{25}@Ni-MOF-74 > Au_{25}@Co-MOF-74 > Au_{25}@Zn-MOF-74 > Au_{25}@Mg-MOF-74 (Fig. 3b). The results indicate that the metal doping in M-MOF-74 exerts a pivotal influence on the catalytic efficiency of $Au_{25}(Cys)_{18}$. Powder XRD patterns of Au_{25}@M-MOF-74 do not exhibit any discernible decrease in the MOF crystallinity after the catalytic reaction (Fig. S14); the UV–vis spectra of the detached Au_{25} NCs upon the MOF removal exhibit no substantial alterations with the as-synthesized Au_{25} NCs, effectively demonstrating the structural integrity of both components in Au_{25}@M-MOF-74 during the catalytic reaction (Fig. 3c). As a control, the Au nanoparticles (NPs) with surface ligands of Cys were synthesized; the UV–vis spectrum displays a characteristic surface plasmon resonance peak at 520 nm and the HAADF-STEM image indicates that the Au NPs are ~2 nm in size (Fig. S15). Afterward, they were encapsulated into Ni-MOF-74 to obtain Au_{NPs}@Ni-MOF-74 with retained Au sizes and good MOF crystallinity (Fig. S16) via the same coordination self-assembly as that of Au_{25}@Ni-MOF-74. The conversion and selectivity of Au_{NPs}@Ni-MOF-74 in the reaction are only 15.2% and 89.5%, respectively (Table S2). This is possibly attributed to the fact that the charge-transfer effect on the surface of Au NPs is too weak to efficiently facilitate the migration of electrons from $NaBH_4$ to the substrate [37].

The incorporation of $Au_{25}(Cys)_{18}$ into M-MOF-74 has been demonstrated to not only influence the activity as noted above, but also strongly improve the catalytic stability. The catalytic yield of Au_{25}@Ni-MOF-74 is maintained at 99% for 1 h in the three cycles; in contrast, the yield of Au_{25}/Ni-MOF-74 gives 25% in the first cycle and decreases continuously during the next two cycles (Fig. S17), possibly due to the unexpected leaching or aggregation of $Au_{25}(Cys)_{18}$. HAADF-STEM images show that the size and dispersion of $Au_{25}(Cys)_{18}$ in Au_{25}@Ni-MOF-74 remain unchanged after three reaction cycles due to the confined protection by the MOF, whereas significant agglomeration of Au_{25} NCs is observed in Au_{25}/Ni-MOF-74 (Fig. S18). No noticeable change occurs in the Au content in Au_{25}@Ni-MOF-74 after the reaction; however, a decrease of ~10% can be found for Au_{25}/Ni-MOF-74 (Table S1). These results exemplify the much enhanced stability of $Au_{25}(Cys)_{18}$ by MOF encapsulation.

The stability and recyclability of Au_{25}@Ni-MOF-74 have been further demonstrated. The activity and selectivity exhibit no significant decrease in the five consecutive cycles with a controlled reaction time of 40 min and ~80% conversion (Fig. 3d). Powder XRD patterns, HAADF-STEM images and corresponding EDS elemental mapping analyses suggest that the catalyst microstructure can be retained after five consecutive cycles (Figs S19 and S20). In addition, the results of the hot filtration experiment for Au_{25}@Ni-MOF-74 manifest that no leaching occurs in Au_{25} NCs and the process is truly heterogeneous catalysis (Fig. S21).

Mechanism of the catalytic reaction

Given the significant differences in the activity of Au_{25}@M-MOF-74, relevant investigations have been conducted to understand the intrinsic mechanisms involved. The variations in fluorescence emission intensity and wavelength can reflect the extent of motion associated with the vibration and rotation of the ligands on the surface of the metal NCs [39,40]. Under excitation of 420 nm, the photoluminescence (PL) spectrum of $Au_{25}(Cys)_{18}$ is in the visible region with a maximum value of ~720 nm (Fig. 4a) and the PL of Au_{25}@M-MOF-74 is substantially enhanced in intensity and undergoes an obvious blue shift compared with that of $Au_{25}(Cys)_{18}$. The phenomenon can be ascribed to the coordination interactions between the metal-oxo chain in M-MOF-74 and the free carboxyl

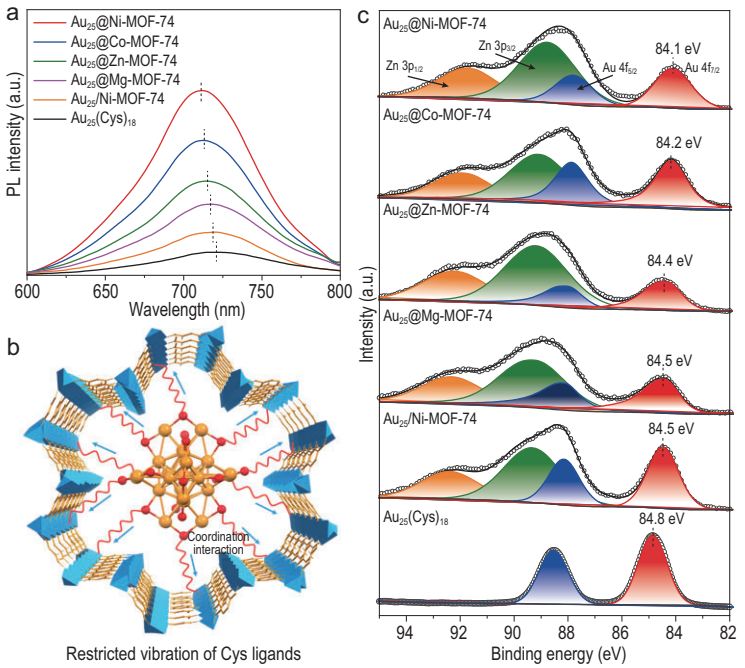

Figure 4. (a) Fluorescence spectra of $Au_{25}(Cys)_{18}$, Au_{25}@M-MOF-74 and Au_{25}@Ni-MOF-74 in aqueous solution. (b) A schematic diagram of encapsulating $Au_{25}(Cys)_{18}$ by M-MOF-74 restricts Cys ligand vibrations on its surface. (c) The Au 4f XPS spectra of $Au_{25}(Cys)_{18}$, Au_{25}/Ni-MOF-74 and Au_{25}@M-MOF-74.

groups from the Cys on the surface of $Au_{25}(Cys)_{18}$, which restricts the vibration and rotation of the Cys ligands and inhibits the non-radiative leaps of $Au_{25}(Cys)_{18}$, thereby improving the emission efficiency [41]. Moreover, this interaction affects the electronic structure of $Au_{25}(Cys)_{18}$, giving rise to the blue shift of its fluorescence signal [39]. Therefore, the PL intensity and peak shift of $Au_{25}(Cys)_{18}$ incorporated in M-MOF-74 can reflect the degree of Cys rigidification (Fig. 4b). The PL intensities and peak shift of $Au_{25}(Cys)_{18}$ follow the trend of Au_{25}@Ni-MOF-74 > Au_{25}@Co-MOF-74 > Au_{25}@Zn-MOF-74 > Au_{25}@Mg-MOF-74, in agreement with the order of their catalytic activities. This reflects that the difference in the coordination strength between the MOF metal-oxo chains with carboxylate groups on the $Au_{25}(Cys)_{18}$ surface modulates the microenvironment of $Au_{25}(Cys)_{18}$, influencing the catalytic activity. The PL intensity and shift of Au_{25}@M-MOF-74 are apparently greater than those of Au_{25}/MOF-74, suggesting that the MOF encapsulation is more favorable for the rigidification of Cys and improves the activity to a larger extent.

X-ray photoelectron spectroscopy (XPS) analysis demonstrates a significant increase in the Au electron density of $Au_{25}(Cys)_{18}$ upon integration with M-MOF-74 (Fig. 4c). Interestingly, the electron density of Au in Au_{25}@M-MOF-74 is in a sequence that is consistent with their activity order, disclosing the fact that the charge-transfer interaction between $Au_{25}(Cys)_{18}$ and M-MOF-74 benefits the activity. In addition, the change in the Au electron density in Au_{25}/Ni-MOF-74 is relatively small, further suggesting that $Au_{25}(Cys)_{18}$ supported on MOF cannot create a strong interaction with $Au_{25}(Cys)_{18}$.

UV–vis spectroscopy and electron spin resonance (ESR) spectroscopy are further adopted to investigate the electron-transfer process in the catalytic reactions. The Au_{25} NCs with different charges have unique UV–vis absorption spectra, which can clearly distinguish the charge states of Au_{25} NCs [42]. When 2-nitrobenzonitrile is added as the substrate to the $Au_{25}(Cys)_{18}$ with a negative charge (abbreviated as Au_{25}^{-}) in the aqueous solution, its UV–vis spectrum displays a distinct change from the characteristic spectrum of uncharged $Au_{25}(Cys)_{18}$ (abbreviated as Au_{25}^{0}). After $NaBH_4$ is added, the characteristic absorption peak of Au_{25}^{-} reappears (Fig. S22), indicating the recovery of Au_{25}^{-}. Furthermore, ESR experiments indicate that Au_{25}@Ni-MOF-74 and the mixture of Ni-MOF-74 with 2-nitrobenzonitrile do not result in any signal, whereas the mixture of $Au_{25}(Cys)_{18}$ or Au_{25}@Ni-MOF-74 with 2-nitrobenzonitrile results in a triple peak corresponding to the N radicals (Fig. S23). These results confirm that $Au_{25}(Cys)_{18}$ is an electronic mediator that continuously transfers electrons from $NaBH_4$ to the substrate. In addition, a range of catalytic experiments with substrate analogs have been performed (Table S3). The functional group of the substrates can be efficiently and completely reduced when the unsaturated group is placed at the ortho position only, suggesting that an intermolecular cascade reaction has occurred. To further investigate the catalytic mechanism, deuterium-labeling experiments are also conducted. When H_2O is replaced by D_2O and $NaBH_4$ is replaced by $NaBD_4$ in the reaction system, the molecular weight of the products detected by using mass spectrometry increases (Fig. S24), implying that H_2O and $NaBH_4$ are involved in the reaction. As a result, reaction paths can be proposed (Fig. S25).

The geometric structure and electronic properties of $Au_{25}(Cys)_{18}$

Given that the X-ray absorption fine structure (XAFS) is sensitive to the structure of metal NCs [43,44], the Au L_3-edge XAFS is adopted to investigate the effect of MOF encapsulation on the geometric structure and electronic properties of $Au_{25}(Cys)_{18}$. X-ray absorption near edge structure (XANES) spectra display obvious differences between the peak profiles of $Au_{25}(Cys)_{18}$ and

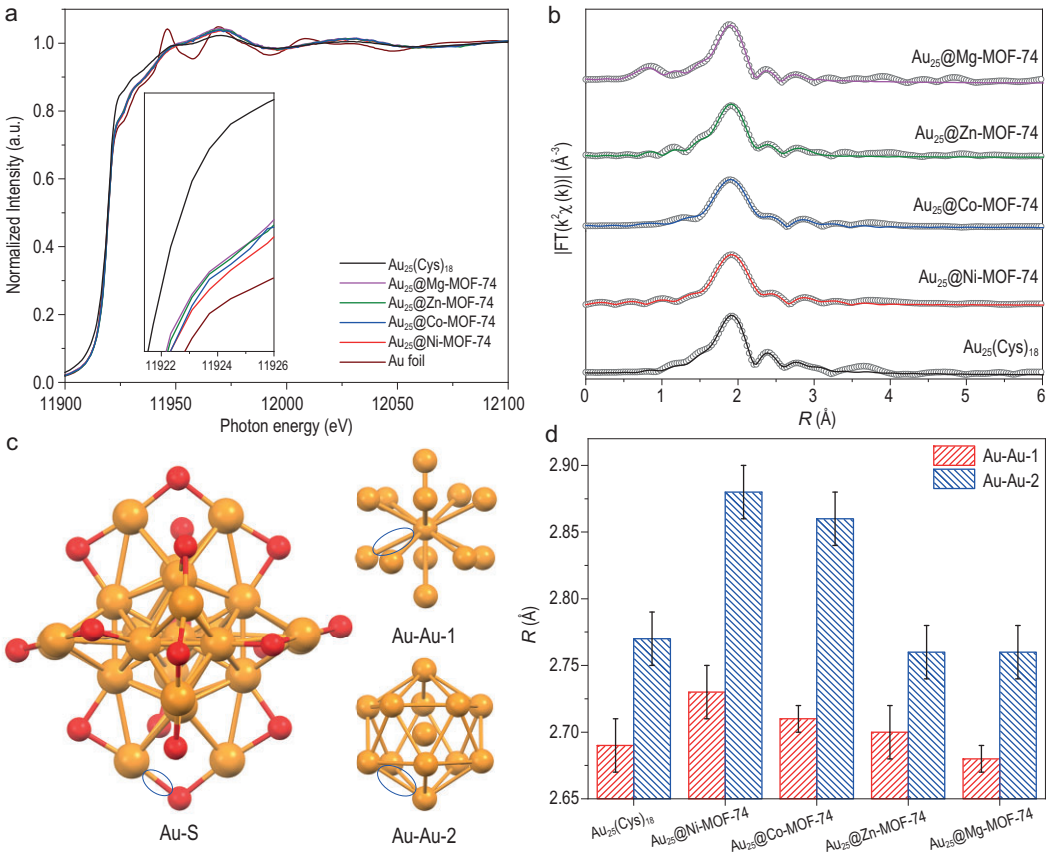

Figure 5. (a) Au L_3-edge XANES spectra of Au foil, $Au_{25}(Cys)_{18}$ and Au_{25}@M-MOF-74. (b) Au L_3-edge FT-EXAFS spectra of $Au_{25}(Cys)_{18}$ and Au_{25}@M-MOF-74. (c) Attribution of the EXAFS-analysed $Au_{25}(Cys)_{18}$ structure to three distinct bond domains (the Au–S, Au–Au-1 and Au–Au-2 highlighted with ellipses). (d) The bond lengths of Au–Au-1 and Au–Au-2 are extracted from the refinement of the FT-EXAFS spectra of $Au_{25}(Cys)_{18}$ and Au_{25}@M-MOF-74.

fcc-structured Au foil (Fig. 5a). Moreover, the peak profile of $Au_{25}(Cys)_{18}$ almost remains after its integration with M-MOF-74, suggesting that the structure of $Au_{25}(Cys)_{18}$ is preserved in Au_{25}@M-MOF-74, which is in agreement with the above results. The white line peak corresponds to the electronic transition from the core level to the unoccupied 5d valence level and the variation in the intensity of the white line peak can drive the absorption edge to different directions of energy, thus explaining different electronic states [45]. In comparison with that of the Au foil, the spectrum of $Au_{25}(Cys)_{18}$ exhibits a more intense white line peak at ∼11 924 eV, which is due to the electron-withdrawing property of the thiol ligand and the reduced 5d electron density of surface Au atoms. On the other hand, the white line intensity of Au_{25}@M-MOF-74 is lower than that of $Au_{25}(Cys)_{18}$, suggesting the greater occupation of the 5d electronic state in Au_{25}@M-MOF-74. This is likely due to the MOF's constraining thiol ligand vibrations on the $Au_{25}(Cys)_{18}$ surface, thereby weakening the electron-withdrawing effect of the thiol ligand toward the Au atoms. In addition, the intensity order of the white line peaks in Au_{25}@M-MOF-74 is further demonstrated by means of differential spectroscopy of XAFS, which is consistent with the results of XPS analysis (Fig. S26), confirming that the microenvironment modulation caused by the interaction between M-MOF-74 and the thiol ligand regulates the Au_{25} electronic structure.

To quantify the local atomic structure of $Au_{25}(Cys)_{18}$ in MOF-74, the extended X-ray absorption fine structure (EXAFS) region has been analysed. All Au_{25}@M-MOF-74 samples exhibit oscillation patterns that are similar to those of $Au_{25}(Cys)_{18}$, whereas the oscillation intensity increases, suggesting that the surrounding microenvironment modulation driven by the MOF encapsulation can affect the degree of $Au_{25}(Cys)_{18}$ disorder (Fig. S27). Fourier transform (FT) is performed in the R-space of the EXAFS spectra for $Au_{25}(Cys)_{18}$ and Au_{25}@M-MOF-74 (Fig. 5b). For $Au_{25}(Cys)_{18}$, three prominent features are shown at 1.9, 2.4 and 2.7 Å; thus, the fittings are

performed using three coordination paths. As previously reported [46], the first peak represents the S atom directly coordinated to Au, i.e. Au–S on the motif of $Au_{25}(Cys)_{18}$, and the other two peaks represent contributions from two Au–Au pathways (Fig. 5c). By comparing the curve-fitting analysis of $Au_{25}(Cys)_{18}$ and Au_{25}@M-MOF-74 EXAFS results (Table S4), it is observed that the bond length of Au–S is very similar (Fig. S28), while Au–Au-1 and Au–Au-2 increase when $Au_{25}(Cys)_{18}$ NCs are encapsulated in Ni-MOF-74 and Co-MOF-74, suggesting that the $Au_{25}(Cys)_{18}$ nucleus undergoes expansion in response to the stronger interaction with M-MOF-74 (Fig. 5d). Notably, the Au–Au bond length sequence in Au_{25}@M-MOF-74 is in good agreement with their catalytic activity, suggesting that the catalytic performance of metal NCs can be optimized by manipulating the metal-oxo chains in M-MOF-74 hosts. Furthermore, the Au L_3-edge XANES and EXAFS spectra of Au_{25}@Ni-MOF-74 after the reaction are similar to those before the reaction (Fig. S29), further supporting that the structure of the Au_{25} NCs in Au_{25}@Ni-MOF-74 barely changes after the catalytic reaction, matching the UV–vis spectra above (Fig. 3c) and demonstrating that MOF encapsulation improves the structural stability of metal NCs.

Based on the above analysis, it can be concluded that the strong coordination interaction between M-MOF-74 and $Au_{25}(Cys)_{18}$ results in the rigidification of surface ligands and the expansion of the Au nucleus. Given that ligand vibrations on the surface of Au_{25} NCs in the reaction solution prevent the substrate from accessing the Au sites, rigidifying the surface ligands and expanding the gold nucleus are expected to increase the available spatial domain for substrate accessibility, thereby boosting activity. Additionally, the different interaction between tunable M-MOF-74 and surface ligands of $Au_{25}(Cys)_{18}$ effectively regulates the electron transfer from the MOF to Au_{25} NCs. Due to the electrophilicity of the nitro and cyano groups in 2-nitrobenzonitrile, metal surfaces with higher electron densities will give stronger interactions with the substrate [47,48]. Overall, optimization of the accessibility and electron density of the Au_{25} NCs facilitates electron transfer with the substrate and promotes the conversion [49].

CONCLUSION

In summary, atomically precise $Au_{25}(Cys)_{18}$ NCs have been successfully encapsulated in M-MOF-74 with different metal nodes through coordination self-assembly, yielding Au_{25}@M-MOF-74 composites for the intramolecular cascade reaction of 2-nitrobenzonitrile. Strikingly, the activity and stability of $Au_{25}(Cys)_{18}$ are significantly enhanced upon being incorporated into MOF-74, surpassing those of Au_{25}/MOF-74. Remarkably, doping different metal species into the metal-oxo chains in MOF-74 showcases significant activity difference in the order of Au_{25}@Ni-MOF-74 > Au_{25}@Co-MOF-74 > Au_{25}@Zn-MOF-74 > Au_{25}@Mg-MOF-74. Both fluorescence and XAFS analyses demonstrate that the engineering of metal-oxo nodes in MOFs gives rise to the rigidification of surface ligands on $Au_{25}(Cys)_{18}$ and induces expansion at the Au nucleus level, improving the accessibility of the Au sites. Moreover, the stronger coordination interaction between M-MOF-74 and $Au_{25}(Cys)_{18}$ further increases the electron density of Au_{25} NCs, which is favorable to the substrate activation, leading to enhanced activity. This work describes improved single electron transfer and metal site accessibility of metal NCs by regulating the interaction between their surface ligands and multivariate MOF hosts, which opens a new avenue for boosting the catalysis of metal NCs by surface microenvironment modulation.

MERHODS

Synthesis of Au_{25}@Zn-MOF-74

Typically, 0.2 mL of aqueous solution of $Au_{25}(Cys)_{18}$ (15 mg/mL) was added to 1 mL of 0.73 M NaOH aqueous solution of DHTP (0.183 mmol) at 25°C. Then, 1 mL of aqueous solution of $Zn(CH_3COO)_2{\cdot}2H_2O$ (0.732 mmol) was mixed with the solution, sonicated for 1 min and stirred for 6 h at 25°C. The precipitate was collected by centrifugation and washed with H_2O and MeOH three times. Finally, the precipitate was soaked in MeOH for 48 h and dried under a vacuum at 60°C overnight.

Synthesis of Au_{25}@M-MOF-74 (M = Ni, Co, Mg)

Typically, 0.2 mL of $Au_{25}(Cys)_{18}$ aqueous solution (15 mg/mL) was added into 1 mL of 0.73 M NaOH aqueous solution of DHTP (0.183 mmol) at 25°C. Then, 1 mL of aqueous solution of $M(CH_3COO)_2{\cdot}4H_2O$ (0.183 mmol) (M = Ni, Co, Mg) and $Zn(CH_3COO)_2{\cdot}2H_2O$ (0.183 mmol) was mixed with the solution, sonicated for 1 min and stirred for 6 h at 25°C. The precipitate was collected by centrifugation and washed with H_2O and MeOH three times. Finally, the precipitate was soaked in MeOH for 48 h and dried under a vacuum at 60°C overnight.

X-ray absorption spectra

The Au L_3-edge XANES and EXAFS experiments were conducted at the 1W1B beamline station in the Beijing Synchrotron Radiation Facility (BSRF) and the BL14W1 beamline station in the Shanghai Synchrotron Radiation Facility (SSRF). All the data were collected in transmission mode. The incident beam was monochromatized using a Si (111) double-crystal monochromator and a harmonic rejection mirror (S4) was used to eliminate harmonics at high X-ray energy levels. Data reduction, analysis and EXAFS fitting were performed using the Athena and Artemis software packages. The energy calibration of the catalysts was conducted using a standard metal foil as a reference, which was measured simultaneously.

SUPPLEMENTARY DATA

Supplementary data are available at *NSR* online.

ACKNOWLEDGEMENTS

We thank the 1W1B station at BSRF and BL14W1 station at SSRF for XAS measurements. This work was partially carried out at the Instruments Center for Physical Science, University of Science and Technology of China.

FUNDING

This work was supported by the National Key Research and Development Program of China (2021YFA1500402), the National Natural Science Foundation of China (22331009 and U22A20401), the Strategic Priority Research Program of the Chinese Academy of Sciences (XDB0450302 and XDB0540000) and the Fundamental Research Funds for the Central Universities (WK2060000038).

AUTHOR CONTRIBUTIONS

H.W. and H.-L.J. conceived the idea. H.W. designed and performed the experiments. H.-L.J. and T.Y. supervised and directed the project; Y.-L.Z. repeated the synthesis and catalytic experiments; H.W. and Y.L. performed TEM experiments. X.-K.L., Z.-H.S. and T.Y. performed XAFS experiments and analysed the data. H.W. and H.-L.J. co-wrote the manuscript. All authors discussed the results and edited the paper.

Conflict of interest statement. None declared.

REFERENCES

1. Li X, Mitchell S, Fang Y *et al.* Advances in heterogeneous single-cluster catalysis. *Nat Rev Chem* 2023; **7**: 754–67.
2. Jing W, Shen H, Qin R *et al.* Surface and interface coordination chemistry learned from model heterogeneous metal nanocatalysts: from atomically dispersed catalysts to atomically precise clusters. *Chem Rev* 2023; **123**: 5948–6002.
3. Zaera F. Designing sites in heterogeneous catalysis: are we reaching selectivities competitive with those of homogeneous catalysts? *Chem Rev* 2022; **122**: 8594–757.
4. Jin R, Li G, Sharma S *et al.* Toward active-site tailoring in heterogeneous catalysis by atomically precise metal nanoclusters with crystallographic structures. *Chem Rev* 2021; **121**: 567–648.
5. Du Y, Sheng H, Astruc D *et al.* Atomically precise noble metal nanoclusters as efficient catalysts: a bridge between structure and properties. *Chem Rev* 2020; **120**: 526–622.
6. Liu X, Cai X, Zhu Y. Catalysis synergism by atomically precise bimetallic nanoclusters doped with heteroatoms. *Acc Chem Res* 2023; **56**: 1528–38.
7. Guan ZJ, Li JJ, Hu F *et al.* Structural engineering toward gold nanocluster catalysis. *Angew Chem Int Ed* 2022; **61**: e202209725.
8. Sakamoto K, Masuda S, Takano S *et al.* Partially thiolated Au_{25} cluster anchored on carbon support via noncovalent ligand–support interactions: active and robust catalyst for aerobic oxidation of alcohols. *ACS Catal* 2023; **13**: 3263–71.
9. Wang X, Zhao J, Eliasson H *et al.* Very low temperature CO oxidation over atomically precise Au_{25} nanoclusters on MnO_2. *J Am Chem Soc* 2023; **145**: 27273–81.
10. Shen H, Wu Q, Asre Hazer MS *et al.* Regioselective hydrogenation of alkenes over atomically dispersed Pd sites on NHC-stabilized bimetallic nanoclusters. *Chem* 2022; **8**: 2380–92.
11. Wang JQ, He RL, Liu WD *et al.* Integration of metal catalysis and organocatalysis in a metal nanocluster with anchored proline. *J Am Chem Soc* 2023; **145**: 12255–63.
12. Liu Z, Tan H, Li B *et al.* Ligand effect on switching the rate-determining step of water oxidation in atomically precise metal nanoclusters. *Nat Commun* 2023; **14**: 3374.
13. Wu Z, Jiang D, Mann AK *et al.* Thiolate ligands as a double-edged sword for CO oxidation on CeO_2 supported $Au_{25}(SCH_2CH_2Ph)_{18}$ nanoclusters. *J Am Chem Soc* 2014; **136**: 6111–22.
14. Küchler A, Yoshimoto M, Luginbühl S *et al.* Enzymatic reactions in confined environments. *Nat Nanotechnol* 2016; **11**: 409–20.
15. Furukawa H, Cordova KE, O'Keeffe M *et al.* The chemistry and applications of metal-organic frameworks. *Science* 2013; **341**: 1230444.
16. Zhou HC and Kitagawa S. Metal-organic frameworks (MOFs). *Chem Soc Rev* 2014; **43**: 5415–8.
17. Zhao X, Wang Y, Li DS *et al.* Metal-organic frameworks for separation. *Adv Mater* 2018; **30**: 1705189.
18. Ebadi Amooghin A, Sanaeepur H, Luque R *et al.* Fluorinated metal–organic frameworks for gas separation. *Chem Soc Rev* 2022; **51**: 7427–508.
19. Sui J, Liu H, Hu S *et al.* A general strategy to immobilize single-atom catalysts in metal-organic frameworks for enhanced photocatalysis. *Adv Mater* 2022; **34**: 2109203.
20. Chen S, Li WH, Jiang W *et al.* MOF encapsulating N-heterocyclic carbene-ligated copper single-atom site catalyst towards efficient methane electrosynthesis. *Angew Chem Int Ed* 2022; **61**: e202114450.

21. Li G, Zhao S, Zhang Y *et al.* Metal-organic frameworks encapsulating active nanoparticles as emerging composites for catalysis: recent progress and perspectives. *Adv Mater* 2018; **30**: 1800702.
22. Yang Q, Xu Q, Jiang HL. Metal–organic frameworks meet metal nanoparticles: synergistic effect for enhanced catalysis. *Chem Soc Rev* 2017; **46**: 4774–808.
23. Zhang Y, Chen S, Al-Enizi AM *et al.* Chiral frustrated lewis pair@metal-organic framework as a new platform for heterogeneous asymmetric hydrogenation. *Angew Chem Int Ed* 2023; **62**: e202213399.
24. Akpinar I, Wang X, Fahy K *et al.* Biomimetic mineralization of large enzymes utilizing a stable zirconium-based metal-organic frameworks. *J Am Chem Soc* 2024; **146**: 5108–17.
25. Wang KY, Zhang J, Hsu YC *et al.* Bioinspired framework catalysts: from enzyme immobilization to biomimetic catalysis. *Chem Rev* 2023; **123**: 5347–420.
26. Zhao Y, Zhuang S, Liao L *et al.* A dual purpose strategy to endow gold nanoclusters with both catalysis activity and water solubility. *J Am Chem Soc* 2020; **142**: 973–7.
27. Kratzl K, Kratky T, Gunther S *et al.* Generation and stabilization of small platinum clusters $Pt_{12\pm x}$ inside a metal-organic framework. *J Am Chem Soc* 2019; **141**: 13962–9.
28. Yun Y, Sheng H, Bao K *et al.* Design and remarkable efficiency of the robust sandwich cluster composite nanocatalysts ZIF-8@Au_{25}@ZIF-67. *J Am Chem Soc* 2020; **142**: 4126–30.
29. Zhu YF, Qiu XY, Zhao SL *et al.* Structure regulated catalytic performance of gold nanocluster-MOF nanocomposites. *Nano Res* 2020; **13**: 1928–32.
30. Luo Y, Fan S, Yu W *et al.* Fabrication of $Au_{25}(SG)_{18}$-ZIF-8 nanocomposites: a facile strategy to position $Au_{25}(SG)_{18}$ nanoclusters inside and outside ZIF-8. *Adv Mater* 2018; **30**: 1704576.
31. Li YM, Hu J, Zhu M *et al.* Confining atomically precise nanoclusters in metal-organic frameworks for advanced catalysis. *Coord Chem Rev* 2023; **495**: 215364.
32. Wang H, Liu X, Yang W *et al.* Surface-clean Au_{25} nanoclusters in modulated microenvironment enabled by metal-organic frameworks for enhanced catalysis. *J Am Chem Soc* 2022; **144**: 22008–17.
33. Cirri A, Hernández HM, Kmiotek C *et al.* Systematically tuning the electronic structure of gold nanoclusters through ligand derivatization. *Angew Chem Int Ed* 2019; **58**: 13818–22.
34. Jiao L, Wang J, Jiang HL. Microenvironment modulation in metal–organic framework-based catalysis. *Acc Mater Res* 2021; **2**: 327–39.
35. Yuan X, Zhang B, Luo Z *et al.* Balancing the rate of cluster growth and etching for gram-scale synthesis of thiolate-protected Au_{25} nanoclusters with atomic precision. *Angew Chem Int Ed* 2014; **53**: 4623–7.
36. Garzón-Tovar L, Carné-Sánchez A, Carbonell C *et al.* Optimised room temperature, water-based synthesis of CPO-27-M metal-organic frameworks with high space-time yields. *J Mater Chem A* 2015; **3**: 20819–26.
37. Chong H, Li P, Wang S *et al.* Au_{25} clusters as electron-transfer catalysts induced the intramolecular cascade reaction of 2-nitrobenzonitrile. *Sci Rep* 2013; **3**: 3214.
38. Zhao J, Ziarati A, Rosspeintner A *et al.* Anchoring of metal complexes on Au_{25} nanocluster for enhanced photocoupled electrocatalytic CO_2 reduction. *Angew Chem Int Ed* 2024; **63**: e202316649.
39. Zhong Y, Zhang J, Li T *et al.* Suppression of kernel vibrations by layer-by-layer ligand engineering boosts photoluminescence efficiency of gold nanoclusters. *Nat Commun* 2023; **14**: 658.
40. Jin Y, Zhang C, Dong XY *et al.* Shell engineering to achieve modification and assembly of atomically-precise silver clusters. *Chem Soc Rev* 2021; **50**: 2297–319.
41. Nie Y, Tao X, Zhang H *et al.* Self-assembly of gold nanoclusters into a metal–organic framework with efficient electrochemiluminescence and their application for sensitive detection of rutin. *Anal Chem* 2021; **93**: 3445–51.
42. Li G, Hu W, Sun Y *et al.* Reactivity and lability modulated by a valence electron moving in and out of 25-atom gold nanoclusters. *Angew Chem Int Ed* 2020; **59**: 21135–42.
43. Yonesato K, Yanai D, Yamazoe S *et al.* Surface-exposed silver nanoclusters inside molecular metal oxide cavities. *Nat Chem* 2023; **15**: 940–7.
44. Ding T, Liu X, Tao Z *et al.* Atomically precise dinuclear site active toward electrocatalytic CO_2 reduction. *J Am Chem Soc* 2021; **143**: 11317–24.
45. Chen Z, Walsh AG, Zhang P. Structural analysis of single-atom catalysts by X-ray absorption spectroscopy. *Acc Chem Res* 2024; **57**: 521–32.
46. MacDonald MA, Chevrier DM, Zhang P *et al.* The structure and bonding of $Au_{25}(SR)_{18}$ nanoclusters from EXAFS: the interplay of metallic and molecular behavior. *J Phys Chem C* 2011; **115**: 15282–7.
47. Shao S, Yang Y, Sun K *et al.* Electron-rich ruthenium single-atom alloy for aqueous levulinic acid hydrogenation. *ACS Catal* 2021; **11**: 12146–58.
48. Nandhakumar P, Kim G, Park S *et al.* Metal nanozyme with ester hydrolysis activity in the presence of ammonia-borane and its use in a sensitive immunosensor. *Angew Chem Int Ed* 2020; **59**: 22419–22.
49. Astruc D. On the roles of electron transfer in catalysis by nanoclusters and nanoparticles. *Chem Eur J* 2021; **27**: 16291–308.